ELSEVIER

Materials Science and Engineering A349 (2003) 48–58

MATERIALS SCIENCE & ENGINEERING A

www.elsevier.com/locate/msea

Mechanical relaxation of localized residual stresses associated with foreign object damage

B.L. Boyce [a,*], X. Chen [b], J.O. Peters [a,1], J.W. Hutchinson [b], R.O. Ritchie [a]

[a] *Materials Sciences Division, Lawrence Berkeley National Laboratory, Department of Materials Science and Engineering, University of California, Berkeley, CA 94720, USA*

[b] *Division of Engineering and Applied Science, Harvard University, Cambridge, MA 02138, USA*

Received 16 May 2002; received in revised form 15 July 2002

Abstract

Foreign-object damage associated with the ingestion of debris into aircraft turbine engines can lead to a marked degradation in the high-cycle fatigue (HCF) life of turbine components. This degradation is generally considered to be associated with the premature initiation of fatigue cracks at or near the damage sites; this is suspected to be due to, at least in part, the impact-induced residual stress state, which can be strongly tensile in these locations. However, recent experimental studies have shown the unexpected propensity for impact-induced fatigue crack formation at locations of compressive residual stress in the vicinity of the impact site. To address this issue, in situ and ex situ spatially-resolved X-ray diffraction and numerical modeling are utilized to show that the initial residual stress state can be strongly relaxed during the fatigue loading process. The magnitude and rate of relaxation is strongly dependent on the applied loads. For a Ti–6Al–4V turbine blade alloy, little relaxation was observed for an applied maximum stress of 325 MPa ($0.35\sigma_y$, where σ_y is the yield stress), and cracks tended to form in subsurface zones of tensile residual stress away from the damage sites. In contrast, at an applied maximum stress of 500 MPa ($0.54\sigma_y$), equal to the smooth-bar 10^7-cycle endurance strength, cracks tended to form at the damage sites in zones of high stress concentration that had initially been in strong compression, but had relaxed during the fatigue loading.

Keywords: Titanium; Ti–6Al–4V; Foreign-object damage; Impact; Residual stress; X-ray diffraction; Fatigue

1. Introduction

The ingestion of airborne objects or debris into aircraft turbine engines can lead to severe reductions in the expected high-cycle fatigue (HCF) life of impact-damaged components [1,2]. In a simplified simulation of such damage using high-velocity impacts of hard spherical objects onto a Ti–6Al–4V blade alloy, studies [3,4] have shown that the endurance strength can be reduced by as much as 50% and the number of cycles to failure at a given stress amplitude decreased by several orders of magnitude. The reduction in fatigue life due to such foreign-object damage (FOD) was reasoned to be associated with four main factors: (i) impact-induced residual stresses, (ii) microcracks formed upon impact, (iii) the stress-concentrating effects of the impact site, and (iv) distortion of the microstructure.

In an effort to specifically quantify the contribution of residual stresses, spatially-resolved synchrotron X-ray diffraction experiments were carried out to measure local residual stress values in the vicinity of the impact sites [5]. While the presence of such local stresses was thought to influence the premature initiation of fatigue cracks and their early growth during subsequent fatigue cycling, these preliminary studies [4–7] indicated the potential relaxation of the impact-induced residual stresses during fatigue loading, implying that in this relaxed state, the residual stresses might not be a

* Corresponding author. Present address: Sandia National Laboratories, PO Box 5800, MS 0889, Albuquerque, NM 87185-0889, USA. Tel.: +1-505-845-7525; fax: +1-505-844-4816.

E-mail addresses: blboyce@sandia.gov (B.L. Boyce), roritchie@lbl.gov (R.O. Ritchie).

[1] Present address: Technical University Hamburg-Harburg, 21071 Hamburg, Germany.

0921-5093/02/$ - see front matter
PII: S0921-5093(02)00543-9

significant driving force (or mitigating force) in crack formation and propagation.

It is the purpose of the current paper to evaluate the redistribution and/or relaxation of impact-induced residual stresses during mechanical fatigue loading using *in situ* and *ex situ* synchrotron X-ray diffraction, to compare the observed behavior with numerical modeling of the damage and subsequent relaxation processes, and to use this information to develop a better understanding of the driving force for the initiation and subsequent propagation of cracks at sites of impact damage during HCF loading.

2. Background

The residual stress state left by the impact of a projectile onto a metallic surface can be significantly altered during subsequent fatigue loading. Such mechanical cycle-dependent redistribution of residual stresses is often termed 'cyclic relaxation' or 'fading', and has been studied predominantly with respect to shot peening and welding induced residual stresses[2]. Although there is little information on single impact damage, multiple impact shot peening studies in steels have identified four

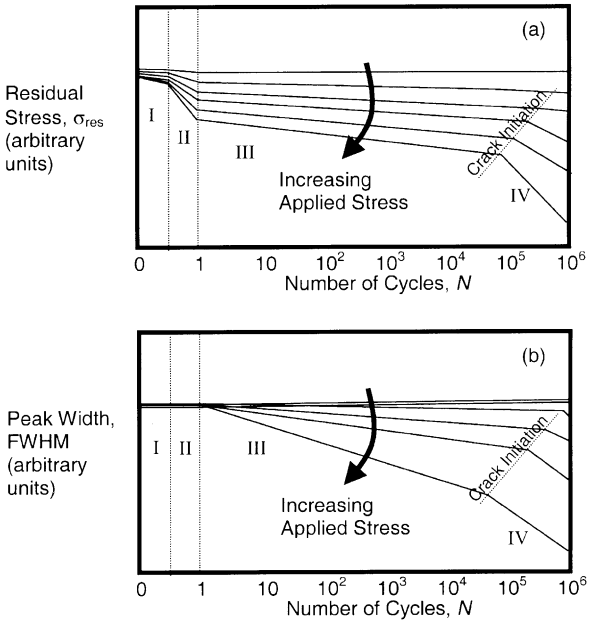

Fig. 1. Schematic illustrations of the relaxation behavior as a function of applied stress observed in shot peened AISI 4140 steel subjected to fully reversed ($R = -1$) fatigue loading, showing (a) relaxation of residual stresses and (b) relaxation of plastic damage as described by the Bragg peak width [9].

regimes of relaxation of the residual compressive stresses under fully reversed loading [8,9] (Fig. 1): (I) the tensile portion of the first cycle, (II) the compressive portion of the first cycle, (III) the subsequent cycles up to crack initiation, and (IV) cycles after crack initiation. During the first cycle, i.e. in regimes I and II, stress relaxation occurs when the superposition of the applied and residual stresses exceeds the yield stress[3]. Thereafter, the residual stresses are often observed to decay at a rate proportional to the logarithm of the number of loading cycles [8,9]. This decay is typically associated with the reordering of the dislocation substructure and is thought to be related to the occurrence of cyclic softening, i.e. the reduction in the flow stress during cyclic loading. Upon the formation of a fatigue crack, however, the relaxation rate can increase, presumably due to the stress-concentrating effect and plasticity associated with the crack. For each of the four regimes, there is a material-dependent threshold stress amplitude below which no relaxation is seen.

In addition to relaxing the residual stresses, fatigue cycling can also cause a decay in the dislocation density or cold work associated with the residual stresses, as shown by a reduction in the Bragg peak width (FWHM). Again, results on steels (AISI 4140) show the Bragg peak width to decay linearly with the logarithm of the number of cycles after shot peening at room temperature [9]. There is a threshold stress amplitude below which the peak-widths are unaltered by cycling. In this steel, the threshold is several hundred MPa higher than the threshold for residual stress relaxation, indicating that at intermediate stress amplitudes, the macroscopic residual stress state can decay with cycling while the degree of plastic damage remains constant. Similar observations have been reported for AISI 304 steel and AZ31 magnesium alloys, where residual stresses relaxed substantially during fatigue loading, whereas, the peak-widths remained essentially constant [10].

Corresponding results on peening-induced residual stresses in titanium alloys, specifically a comparison of 'near-α' IMI-685 (in a β annealed condition) and α+β Ti–6Al–4V (in a condition similar to that of the present study), show the marked effect of cyclic deformation properties on relaxation [11]. In IMI-685, which undergoes very little cyclic softening, cycling at a maximum stress of $0.75\sigma_y$ (where, σ_y is the yield stress) led to a small ($\sim 10\%$) reduction in the peak longitudinal stress. In contrast, cycling IMI-318 at $0.83\sigma_y$ caused a much larger ($\sim 60\%$) reduction, consistent [12] with the fact

[2] It should be noted that the term 'relaxation' can also be used to refer to thermally-driven redistribution of residual stresses. This is a separate driving force from the purely mechanical relaxation discussed herein.

[3] The yield stress referred to in stage II (where the applied and residual stresses are of an opposite sense) is the reverse yield stress; its magnitude is often smaller than the monotonic yield stress due to the Bauschinger effect.

that this alloy experiences substantial cyclic softening. It is thought that this difference in softening behavior is more related to the differences in the microstructure and not as much due to differences in chemical composition.

3. Approach

3.1. Material

The material studied in this investigation was a Ti–6Al–4V alloy with composition (in wt.%) of 6.30 Al, 4.17 V, 0.19 Fe, 0.19 O, 0.013 N, 0.0035 H, bal. Ti. It was received as 20 mm thick forged plates from Teledyne Titanium after solution treating 1 h at 925°C and vacuum annealing for 2 h at 700°C. This alloy, which has been chosen as the basis of a comprehensive military/industry/university program on High Cycle Fatigue, has a microstructure consisting of a bimodal distribution of ~60 vol.% primary-α and ~40 vol.% lamellar colonies of α+β (Fig. 2)[4]. At ambient temperatures this structure displays yield and tensile strengths of 930 and 970 MPa, respectively, and a Young's modulus of 116 GPa [13].

Prior to impact or quasi-static indentation, specimens were machined from the as-received plates into a threaded tensile dogbone geometry (similar to the so-called K_b bar geometry), as shown in Fig. 3. After machining, surface damage was minimized by a standard chemical milling procedure (H_2O, HNO_3, and HF in a ratio of 30:10:1 at ambient temperature), followed by a stress-relief anneal at 700°C for 2 h (with a helium cool).

3.2. Simulation of foreign object damage

As in our previous studies [4–7], FOD was simulated by firing Cr-hardened steel spheres of diameter 1 or 3.2 mm at the flat, nominally stress-free surface of the dogbone specimens at velocities of 200 to 300 m/s using a compressed-gas gun. For comparison, similar states of damage were also induced using quasi-static indentation. A 3.2 mm diameter sphere was indented into the surface to a maximum load of 9 or 22 kN to produce a residual indent with dimensions equivalent to those produced by dynamic 200 or 300 m/s impacts, respectively. Interestingly, the residual stresses for the quasi-static indentations were larger than for the dynamic impacts, especially at the key locations of the crater floor and rim; however, no microcracking was observed around the rim of the indents, as is seen during dynamic impact in this alloy [4]. Since the quasi-static indentations generated the higher compressive and tensile residual stresses, this method, rather than dynamic impacting, was principally used in the present study of the relaxation of the residual stresses during subsequent fatigue cycling.

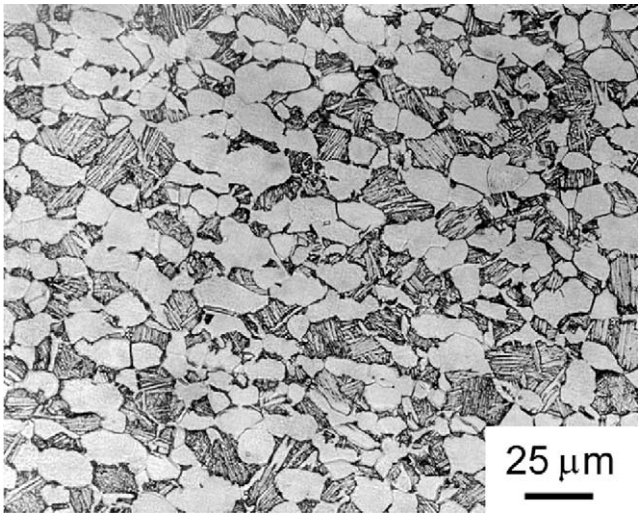

Fig. 2. Optical micrograph of the two-phase microstructure of the bimodal Ti–6Al–4V forged plate alloy, consisting of the hexagonal closed-packed α-phase and body-centered cubic β-phase. Kroll's etchant preferably attacks the phase boundaries of globular and lamellar alpha phase giving contrast to optical microscopy. The α-phase exists in both the globular primary-α phase and in the lamellar colonies of alternating α and β (etched in 3.5% HNO_3–5% HF).

3.3. Fatigue loading

3.3.1. Ex situ residual stress measurements

Following indentation, specimens were subjected to a fatigue loading at a fixed stress ratio $R = \sigma_{min}/\sigma_{max} = 0.1$

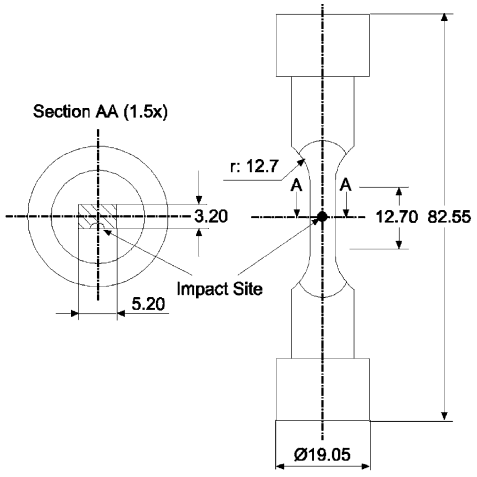

Fig. 3. Tensile dogbone specimens in the so-called K_b geometry typically used to mimic the purely tensile fatigue loading condition of centrifugally-loaded rotating blades. All dimensions are in millimeters.

[4] In the context of the Air Force High Cycle Fatigue program, this microstructure in Ti–6Al–4V has been referred to as 'solution treated and overaged' (STOA).

with a constant applied maximum stress, σ_{max}, of 500 MPa ($0.54\sigma_y$) or 325 MPa ($0.35\sigma_y$). About 500 MPa represents the smooth-bar 10^7-cycle endurance strength (or fatigue limit) at this load ratio in this alloy [4–7]. Specimens were cycled on an automated MTS servo-hydraulic testing machine, and periodically removed for residual stress measurements after one, ten, 100, and 1000 cycles. Stresses were measured at two specific locations at the damage sites, namely the crater floor and rim; both locations represent potential initiation sites for fatigue failure [4–7]. The crater floor was of particular interest because moderately high compressive stresses were found for the initial residual stress state; such stresses are seemingly inconsistent with observations that fatigue cracks generally initiated at this location following lower velocity (200 m/s) impact damage.

3.3.2. *In situ residual strain measurements during cyclic loading*

In a separate set of experiments, the first several cycles were applied in an in situ tensile loading frame that permitted the X-ray diffraction experiments to be performed on the specimen under loads up to 12 kN. In this way, the response of the residual stresses to cyclic loading could be monitored at several steps along the fatigue cycle, specifically at $N = 0$, 0.2, 0.5, 1, 1.5, 10, and 5000 cycles. (The latter 5000 cycles were not applied in situ). In this experiment the mode of characterization focused on establishing a spatial map of the surface normal strains (ε_{zz}) and the Bragg peak widths as they evolved during fatigue loading.

3.4. *Experimental evaluation of residual stress and strain gradients*

Spatially resolved residual stress measurements were performed using synchrotron X-ray diffraction at beamline 2–1 of the Stanford Synchrotron Radiation Laboratory. The advantage of the synchrotron source for this particular application was the low divergence (< 0.2 mrad) source/detector configuration to minimize sample displacement errors associated with the coarse topography of the indent, and a photon flux several orders of magnitude more intense than a conventional sealed-tube source, enabling spatial resolution on the order of a few hundred micrometers without the divergence of capillary optics.

Two modes of characterization were utilized. A relatively fast measurement of the lattice-plane d-spacings normal to the surface, $d_\perp$, yielded an estimate for the residual elastic strain component, ε_{zz}, normal to the surface, when compared with the unstressed lattice constant, d_0. Application of Bragg's law indicates that this surface normal strain is related to the ratio of the sines of the unstressed and stressed Bragg angles, θ_0 and θ, respectively:

$$\varepsilon_{zz} = \frac{d_\perp - d_0}{d_0} = \frac{\sin\theta_0}{\sin\theta} - 1. \quad (1)$$

As these measurements do not yield values for any of the stress components (without additional restrictions on the stress state), the conventional $\sin^2\psi$ method [14,15] was used to interrogate specific locations at the damage sites, namely, the crater rim and floor. This method permits measurement of the individual stress components with a precision that is much less sensitive to the exact value of the d-spacing. In this technique, the diffraction vector is tilted away from the surface normal at various angles ψ. In many cases, the d-spacing varies linearly with $\sin^2\psi$ (hence, the name of the technique); in these instances, the slope of this variation can be related to the stress component along the direction of the diffraction vector at $\psi = 90^\circ$ via the X-ray elastic constants (typically characterized experimentally for a particular Bragg reflection):

$$\frac{d_\psi - d_0}{d_0} = \frac{1+\nu}{E}\,\sigma_{\psi=90}\sin^2\psi - \frac{\nu}{E}(\sigma_{\gamma\gamma} + \sigma_{\theta\theta}). \quad (2)$$

Independent validation of both the out-of-plane strain measurement technique and the $\sin^2\psi$ technique was achieved by applying known strain levels to a standard, similar to that used in previous diffraction-based residual stress studies [15]. A strain-gauged Ti–6Al–4V tensile specimen was loaded in an in situ tensile load frame to various levels of strain ranging from 0 to 6000 $\mu\varepsilon$ corresponding to uniaxial stresses in the range of 0–700 MPa. The elastic strains measured by the X-ray method were found to be within 300 $\mu\varepsilon$ of the observed strain gauge values.

3.5. *Numerical methods for estimating residual stress states*

The numerical simulation was performed with the finite element method (FEM) using the commercial ABAQUS code [16]. To make connection with experiments, the exact specimen geometries were used. A typical mesh for the three-dimensional indentation model comprised more than 54 000 27-node three-dimensional brick elements (with reduced integration). The rigid contact surface option was used to simulate the rigid indenter, and the option for finite deformation and strain employed. Coulomb friction was invoked in the calculations, with the friction coefficient taken to be 0.1.

The hardening law used for the Ti–6Al–4V alloy was defined taking into account the Bauschinger effect. In continuum mechanics, this effect is conveniently regarded as a nonlinear isotropic/kinematic (mixed) hardening material feature in a constitutive model. With the

reduction in flow stress after a reversal in strain direction, additional plastic deformation can occur at relatively low applied cyclic load. Consequently, both compressive and tensile residual stresses are relaxed. In the present work, the flow rule of the mixed hardening model consisted of two components: a purely kinematic hardening term, which describes the translation of the yield surface in stress space through the backstress tensor, α, and an isotropic hardening term, which relates the size of the yield surface with the accumulated plastic deformation. Throughout, the kinematic hardening law was taken as [16]:

$$\dot{\alpha}_{ij} = C\frac{\sigma_{ij} - \alpha_{ij}}{\sigma_0}\,\dot{\bar{\varepsilon}}^p - \gamma\alpha_{ij}\dot{\bar{\varepsilon}}^p \tag{3}$$

where

$$\dot{\bar{\varepsilon}}^p = \sqrt{\frac{2}{3}\dot{\varepsilon}^p_{ij}\dot{\varepsilon}^p_{ij}}$$

is the equivalent plastic strain rate and σ_0 is the equivalent stress defining the yield surface. C and γ are material parameters; both equal zero for isotropic hardening. The size of the yield surface, σ_0, is a function of $\bar{\varepsilon}^p$ through isotropic hardening.

Experimentally, the Bauschinger effect was characterized by conducting a symmetric strain-controlled cyclic experiment at a strain range $\Delta\varepsilon = \pm 3\%$. The resulting uniaxial stress–strain relationship taken over five load cycles is shown in Fig. 4. A functional fit to these data yielded kinematic hardening parameters of $C = 1.38 \times 10^{11}$ and $\gamma = 635$. It is apparent that the Bauschinger effect in this alloy is fairly large, i.e. the reversed yield stress is small (0.2% offset yield of -600 MPa compared with 930 MPa for monotonic loading), such that the non-linearity of the cyclic stress–strain behavior is fairly strong. The stabilized constitutive relationship was, thus, obtained after just two load cycles and behaved essentially the same as kinematic hardening.

To perform the calculation, after the initial indentation, a number of loading cycles at an applied maximum stress of $\sigma_{max} = 325$ MPa (or 500 MPa) at $R = 0.1$ was applied to the specimen, with the cyclic stress acting in the longitudinal direction. The calibrated Bauschinger effect was incorporated into the three-dimensional finite element program by using the empirical data from Fig. 4. The predictions from numerical simulations are compared with the corresponding experimental measurements in Section 4.3

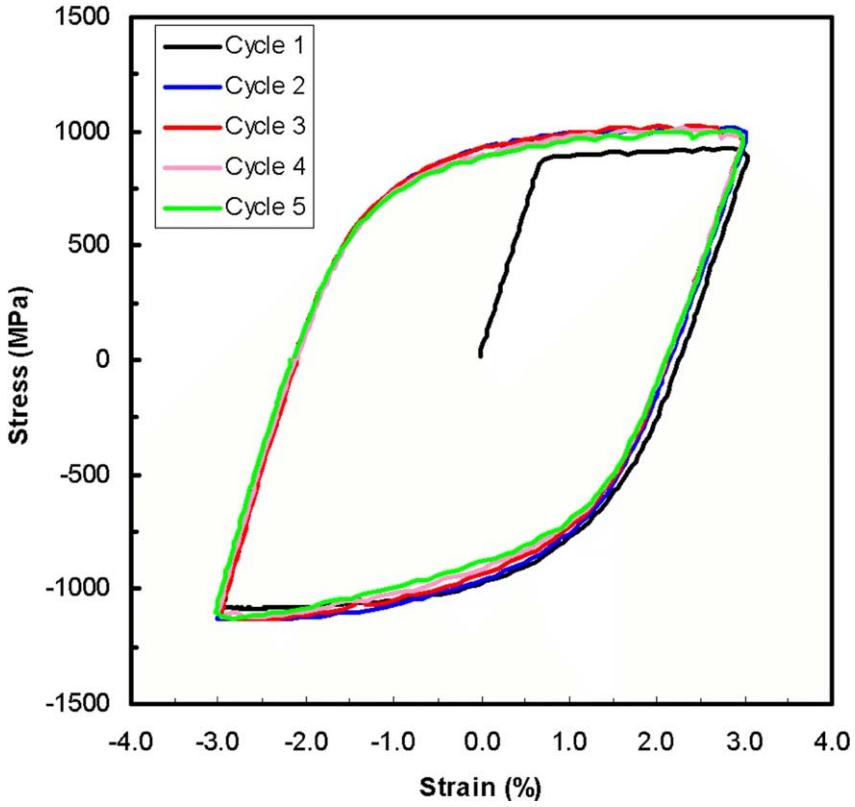

Fig. 4. Experimentally measured cyclic uniaxial stress–strain behavior of the Ti–6Al–4V alloy loaded under strain control to a total strain $\pm 3\%$ for five cycles. Strain was measured axially in the gage section using an extensometer.

4. Results and discussion

4.1. Initial residual stress state

The initial residual stress state, prior to fatigue loading, due to the impact or quasi-static indentations has been determined previously by a combination of experimental X-ray diffraction and finite element analysis [5,17], however, it is worthwhile to emphasize some key features of this residual stress distribution here. An overview of the general shape of the residual stress field, illustrated in Fig. 5, reveals two primary zones of tension in the immediate vicinity of the indent, namely (i) a small but intense region at the surface immediately outside the crater rim, and (ii) a broader region approximately one crater radius away from the impact site where the maximum stresses are well below the surface. The most substantial compressive stresses, which counterbalance the regions of residual tension, are formed in a large zone directly beneath the crater, and show a maximum of approximately 1.5 times the yield stress at roughly one crater radius below the crater floor. The residual stresses remain compressive at the surface of the crater floor, although they are substantially smaller.

While the absolute magnitudes of the stresses are affected by whether the indentation is achieved quasi-statically or dynamically, the general features of the residual stress field are the same in both cases. In the present study where the quasi-static indentation of a K_b tensile specimen was examined, the resulting indent had a diameter of 2.05 mm and a depth of 300 μm, i.e. similar to the size of an indent produced dynamically at an impact velocity of 200 m/s. With this configuration, quantitatively the initial residual stress state before fatigue cycling consisted of compressive residual stresses at the crater floor of magnitude $-0.50\sigma_y$, tensile hoop stresses at the crater rim of magnitude $0.45\sigma_y$ and compressive radial stresses at the rim of $-0.40\sigma_y$.

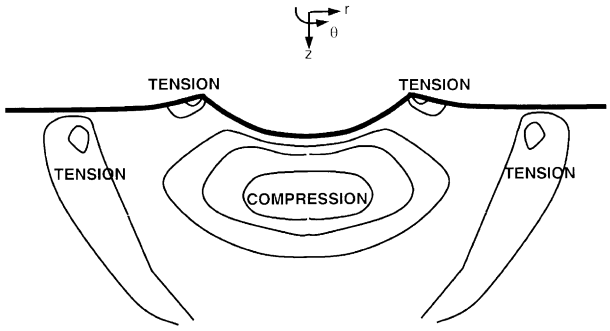

Fig. 5. General shape of the residual $\sigma_{\theta\theta}$ stress field associated with a hemispherical damage site. This hoop stress component is the component that acts in the direction of the subsequent applied fatigue loading (and, thus, to first approximation would superimpose on the applied fatigue stresses). Both quasi-static and dynamic impacts produced similar stress fields, although the magnitudes of the stresses are different. Stress field is based on the FEM analysis of Chen and Hutchinson [17] and consistent with spatially-resolved residual stress measurements on the surface [9].

4.2. Baseline response of undamaged surface state

It is known from studies in both high-strength aluminum alloys [18,19] and SAE 1040 steel [20] that fatigue loading by itself can induce surface residual stresses due to inhomogeneous flow of the material. To evaluate the evolution (if any) of such fatigue-induced residual stresses, a nominally stress-free surface was cycled under identical conditions as used for the mechanically damaged samples in this study, i.e. at $\sigma_{max} = 325$ or 500 MPa (~ 0.3 or $0.5\sigma_y$) at $R = 0.1$. However, over the range of cycles of interest, i.e. over the first 1000 cycles, no alteration in the surface residual stress state induced by the applied load levels could be detected. Consequently, this effect was not considered further in this study.

4.3. Evolution of residual stress state during fatigue loading

For the quasi-static indents, of a size matched to that of a 200 m/s impact, the numerically predicted and experimentally measured change in residual stress levels due to fatigue loading at applied maximum stresses of $\sigma_{max} = 325$ ($\sim 0.3\sigma_y$) and 500 MPa ($\sim 0.5\sigma_y$) is shown in Fig. 6. It is apparent that due to the additional plastic deformation induced by the applied cyclic loads:

- the residual stresses, both at the crater floor and crater rim, were reduced, i.e. the rim stresses became less tensile and the crater floor stresses less compressive,
- the effect was most significant for the higher applied stress level ($\sigma_{max} = 500$ MPa),
- the longitudinal residual stresses (along the direction of loading) were subject to the most relaxation,
- the vast majority of the effect occurred in the first cycle, with little evidence of a continuous decay over subsequent cycles.

Indeed, by cycling at a σ_{max} of 500 MPa, the longitudinal residual stresses were reduced by as much as 50% within the first cycle; the transverse stresses were also reduced, but only by $\sim 20\%$. With further cycling out to 1000 cycles, there was little, if any, additional change in the residual stress state at the floor or the rim of the damage sites. Here, an improved stress resolution may have revealed a very slight decay, although the current observations show almost no change in residual stress levels over three decades in life. Moreover, the

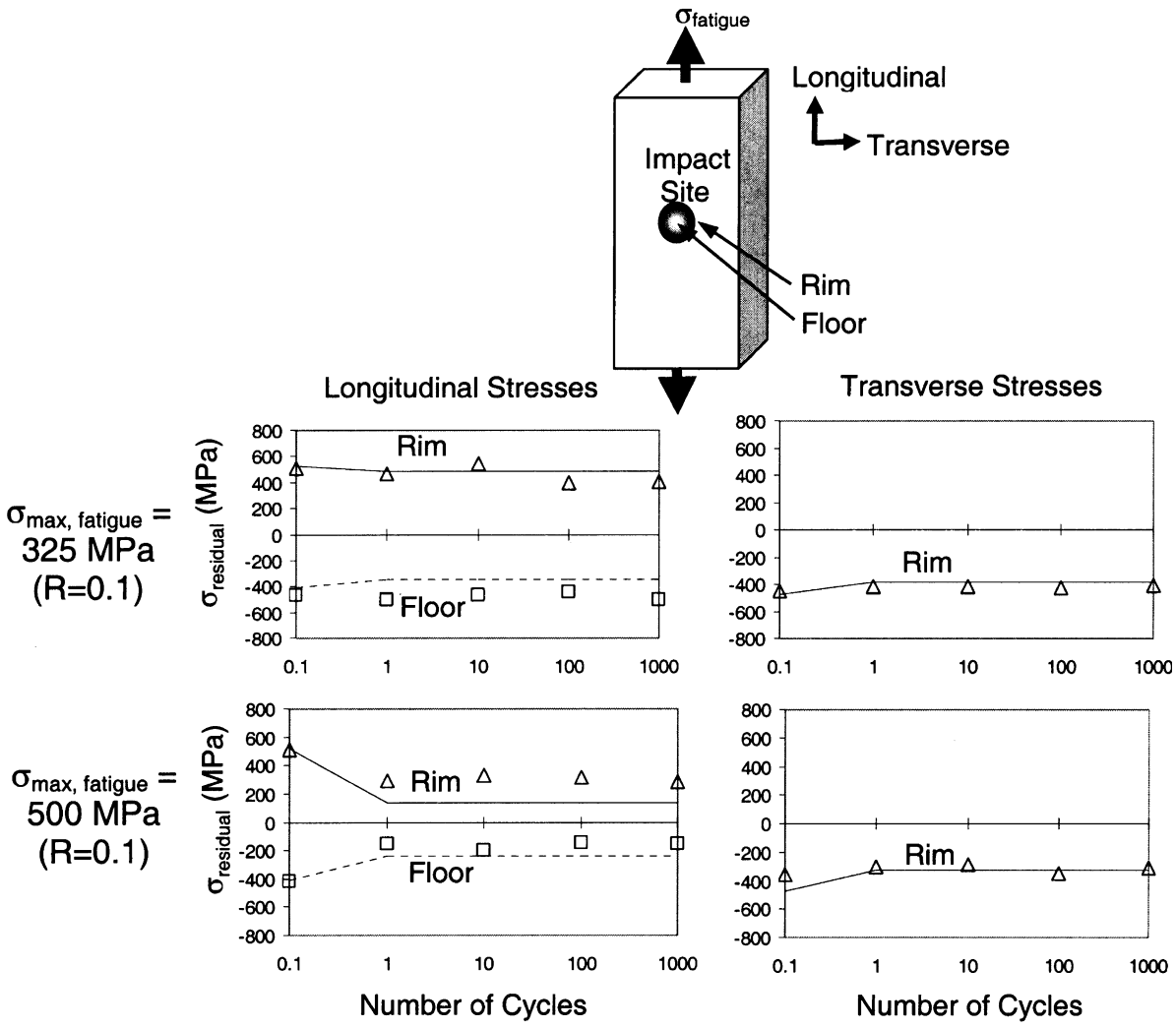

Fig. 6. Cyclic response of the residual stresses at the floor and rim of the damaged crater, following fatigue loading at two maximum stress levels of 325 and 500 MPa at $R = 0.1$. Results are represented both by the FEM predictions (lines) and the spatially-resolved X-ray diffraction measurements (points). It is apparent that the most significant relaxation occurred during the first cycle, and for the highest applied stress level.

numerical and experimental results in Fig. 6 give an identical result in this regard.

It should be noted that the maximum applied stress is small compared with the yield stress ($\sigma_{max}/\sigma_y < 0.6$) and the stress-concentration factors associated with the indent are typically in the range 1.15–1.5. Consequently, in the absence of the Bauschinger effect, the plastic deformation and ensuing relaxation of the residual compressive stress would not have occurred. We, therefore, conclude that the Bauschinger effect and nonlinear cyclic stress–strain behavior of Ti–6Al–4V represent the primary reason behind the fatigue-induced relaxation of the residual stresses in the vicinity of the damage sites. The Bauschinger effect is especially significant in this particular alloy, where the reverse yield stress is quite small compared with the forward yield stress. Specifically, the reverse yield stress is −600 MPa estimated using the 0.2% offset method and first deviation from linearity occurs almost immediately upon compression at values −20 MPa compared with the forward yield stress of 930 MPa. The first-cycle relaxation occurs when the superposition of applied and residual stresses exceed the appropriate yield condition, leading to some plastic accommodation of pre-existing elastic strains associated with the initial residual stress state. The impact-induced residual stresses can be thought of simply as an elastic clamp bearing down on a plastically oversized region, or a plastic clamp contained in an elastic region, with the relaxation attributed to plastic accommodation of initial incompatibility between the elastic and plastic regions.

These observations are consistent with the existing literature on mechanical relaxation [8,9,11]. Specifically, at sufficiently low applied stresses, relaxation is either minimal or completely absent, as shown by behavior at $\sigma_{max} = 325$ MPa ($\sim 0.3\sigma_y$). In contrast, at intermediate

applied stresses, relaxation is almost entirely associated with the first cycle of loading, again as shown by the present study at 500 MPa ($\sim 0.5\sigma_y$). Although not captured in finite element model which does not take into account the localized reordering of the dislocation substructure, the observed relaxation of stresses did not progress, with logarithmic decay, much beyond this first cycle; such behavior is generally associated with much higher applied cyclic stresses closer to the yield stress, and with the development of significant cyclic softening with continued cycling [8,9]. This apparent lack of any decay in residual stress after the first cycle may have been due to the fact that residual stresses were only characterized in the present study during the first $\sim 1\%$ of the total fatigue life. Moreover, unlike the case of fully reversed loading as in [8,9], the $R = 0.1$ condition of the current study incorporates a mean stress component in fatigue loading. After the first cycle, the local mean and maximum stresses at the impact crater would have been reduced by the yielding incurred upon the first cycle. This effect may have further diminished the driving force for relaxation after the first cycle.

4.4. Spatial maps of evolving surface-normal strain and peak widths

To further probe the spatial redistribution of the stress state caused by relaxation, a specimen of the same nominal starting conditions (a quasi-static indent with dimensions identical to those caused by a 200 m/s impact) was loaded using the in situ loading rig. The surface-normal strain distribution was mapped in a quadrant around the indent at several load levels during the first cycle and subsequent cycles up to 5000 cycles, as shown in Fig. 7. From this figure, it is apparent that at a low initial applied stress (σ_{applied}) of 200 MPa ($\sim 0.2\sigma_y$), the residual strain distribution has merely been amplified by the applied stresses. However, at higher loads, there appears to be a distortion in the residual stress state most notably in the reduction in elastic strain at the center of the crater. When the applied stress reaches 500 MPa ($\sim 0.5\sigma_y$), the crater floor undergoes local yielding due to the superposition of the residual stresses and the applied stress multiplied by the stress-concentration factor in this location (~ 1.5). A von Mises estimate for the required applied stress to exceed local yielding at the surface is indeed in the vicinity of 500 MPa. At the lower applied stress of 200 MPa, stress relaxation did not occur as the local stresses were not sufficient to cause yielding in this location.

During unloading of the first cycle there is a further slight decay or redistribution in the strain map, albeit much less pronounced than during the loading portion of the cycle. The strain maps at 1 and 10 cycles look very similar, supporting the notion that the redistribution occurs almost entirely in the first cycle. However, there does appear to be some small degree of further redistribution between 10 and 5000 cycles.

Also of interest are the spatial maps of the Bragg peak widths (FWHM) that give an indication of the degree of plasticity; these are plotted along side the strain maps in Fig. 7. During loading in the first cycle, some broadening of the Bragg peak can be seen, which is most pronounced in the center of the crater where the stress-concentration factor is the highest. Nevertheless, by the end of ten cycles, the peak widths return to their initial values (or even slightly below), and are essentially stabilized with little evidence of further evolution out to 5000 cycles. This indicates that the nature of the plasticity, e.g. dislocation substructure, is not significantly altered by the fatigue cycles under these loading conditions. Therefore, one can conclude that the fatigue initiation and growth characteristics are only altered by the relaxing residual stresses, and not by a relaxation of the plastic damage due to fatigue loading. Here again, under higher applied stresses (not considered in this study), this relaxation of plastic damage would likely ensue and its evolving role on the fatigue behavior should be considered.

5. Implications for foreign object damage

Recent studies [4–7] on the effects of simulated foreign object damage on the HCF behavior of Ti–6Al–4V have shown that for applied cyclic stresses of $\sigma_{\max} = 500$ MPa ($\sim 0.5\sigma_y$), fatigue cracking tends to initiate at the damage crater rim for the highest velocity (300 m/s) impacts and at the crater floor for the lower velocity (200 m/s) impacts. Although the stress concentration associated with the crater is smaller at the rim compared with the floor ($k_{\text{t,floor}} \sim 1.5$, $k_{\text{t,rim}} \sim 1.15$), fatigue cracks initiate there after higher impact velocities due to the presence of impact-induced microcracking. At lower velocities (and for quasi-statically loaded indents), such microcracking is absent and the higher stress-concentration factor at the floor of the crater promotes fatigue crack initiation there instead. When considering the presence of the residual stresses, this latter conclusion is at first sight somewhat surprising because of the relatively high compressive residual stresses of -400 MPa ($-0.4\sigma_y$) initially present at the crater floor, compared with the substantial tensile stresses of 500 MPa ($0.5\sigma_y$) at the crater rim. However, the current observations provide a feasible explanation why crack initiation can occur in this location by revealing an immediate relaxation of these compressive residual stresses on fatigue cycling at 500 MPa.

At lower applied stresses ($\sigma_{\max} = 325$ MPa) where relaxation is far less pronounced, cracks no longer form at the crater floor of lower velocity and quasi-static impact sites, presumably due to the presence of un-

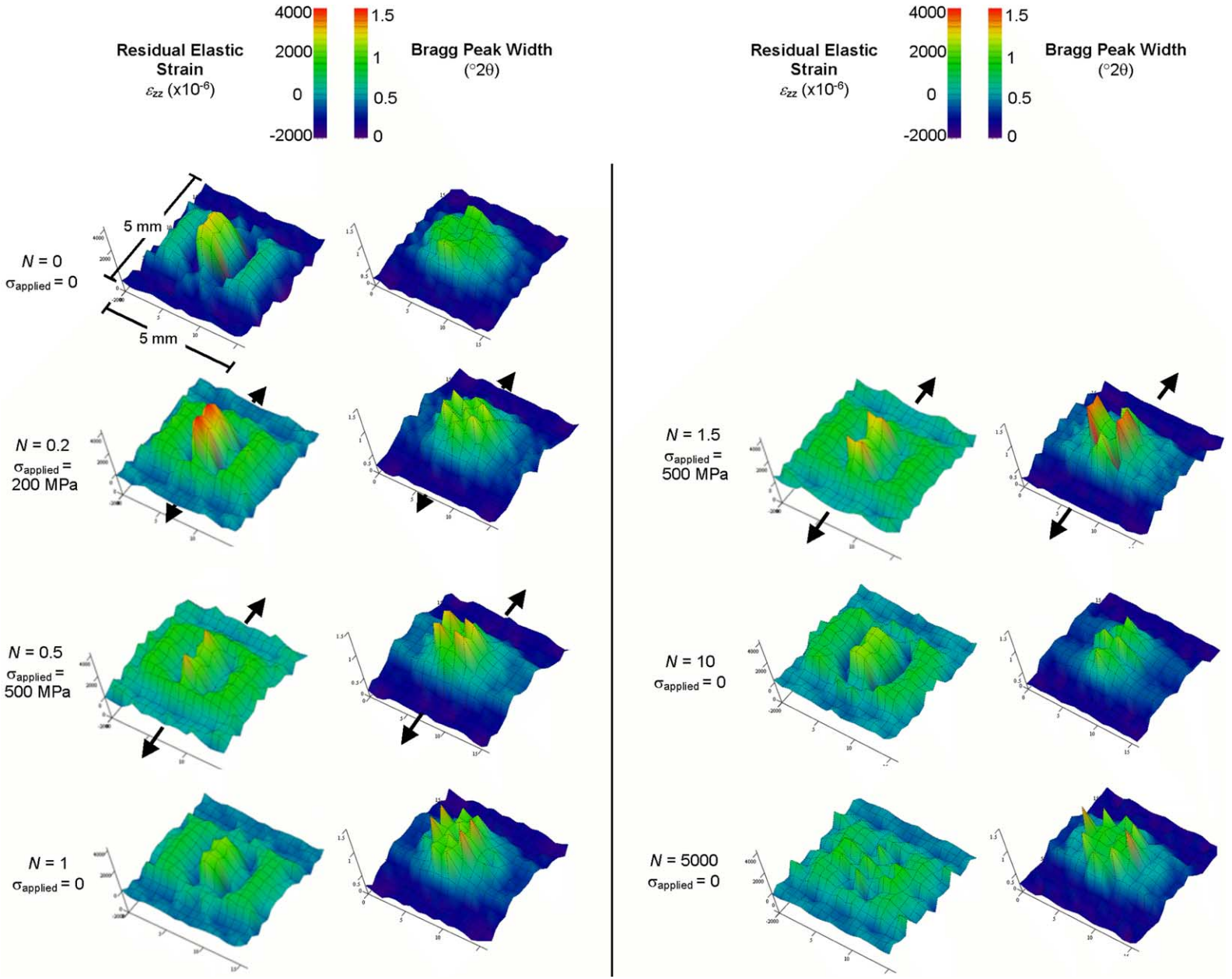

Fig. 7. In situ X-ray diffraction measurements showing the surface-normal strain (left column) and Bragg peak width (FWHM) maps (right column) for a quasi-static loaded indent (equivalent in dimension to a 200 m/s impact) during the process of subsequent fatigue cycling out to $N = 5000$ cycles.

relaxed compressive stresses there. In these instances, fatigue cracks tend to initiate at subsurface regions of residual tension at the side of the crater (see Fig. 5) [4]. Numerical calculations, confirmed by X-ray diffraction experiments, suggest that the residual tensile stresses present in this subsurface zone are on the order of 370 MPa ($\sim 0.4\sigma_y$). By considering the sum of the (marginally relaxed) residual stresses and stress-concentration corrected applied stresses along the direction of loading, the resultant stresses in this region are comparable with those at the crater rim; however, as the rim tensile zone is considerably smaller and surrounded by a zone of compression, this may promote crack formation in the much broader subsurface zone of tensile residual stresses at the side of the indent.

It should be noted here that the presence of such unrelaxed residual stresses does not necessarily change the primary driving force for fatigue crack initiation or growth, i.e. the amplitude of the local stress and strain; however, it does change the local mean stress and strain, and, hence, the local load ratio R, which can still have a significant effect on the limiting conditions for crack initiation and growth.

From a perspective of how this information can be used to develop design rules for the onset of FOD-induced HCF failures in blade alloys such as Ti–6Al–4V, our previous work [4] has demonstrated the utility of the Kitigawa–Takahashi approach [21] in evaluating the limiting conditions for such failures. Where applied stresses are high and comparable with the magnitude of the residual stress, such that significant stress relaxation occurs and fatigue cracks are initiated directly at the impact site, the limiting threshold conditions for HCF failures can be defined in terms of the stress-concentration corrected (smooth-bar) fatigue limit at microstructurally-small crack sizes and a 'worst-case' (large-crack) fatigue-crack growth threshold at crack sizes larger than the scale of microstructure. For smaller applied stresses where significant stress relaxation does not occur and fatigue cracks are initiated away from the impact site, an additional correction must be made to the local load ratio to allow for the presence of the stable residual stresses. Using this approach, described in more detail in [4], 'threshold' stresses for the likelihood of HCF failure can be defined in the aftermath of FOD.

6. Conclusions

Based on a numerical (finite element analysis) and experimental (synchrotron X-ray diffraction) evaluation of the fatigue loading-induced relaxation of localized residual stresses formed around a site of simulated FOD in a forged Ti–6Al–4V alloy, the following conclusions can be drawn.

1) The initial residual stress state associated with FOD can decay during subsequent mechanical loading, e.g. by fatigue, and, therefore, may only have a limited bearing on the driving forces for crack initiation and growth. The degree and rate of this relaxation of residual stresses is dependent on the magnitude of the applied stresses (in relation to the yield stress) during the fatigue cycling.
2) At a low applied maximum stress of 325 MPa (equivalent to 35% of the yield strength σ_y), where the local stresses at the impact crater floor and rim were computed to be 0.50 and $0.42\sigma_y$, respectively, only a slight mechanical relaxation in the damage-related residual stresses was observed.
3) At a higher applied stress of 500 MPa ($0.54\sigma_y$), the smooth-bar fatigue limit, where the local stresses at the floor and rim were, respectively, 0.78 and $0.64\sigma_y$, significant relaxation was seen, with the longitudinal residual stresses, i.e. along the loading direction, decaying by as much as 50% from their initial values. This decay was observed only during the first cycle; subsequent cycles showed little, if any, further relaxation. The lack of a logarithmic decay in residual stresses with number of cycles, as has been reported for shot-peened steels, was reasoned to be associated with the lower applied stresses (compared with the yield stress) utilized in the current study.
4) Numerical modeling which incorporated the experimentally-determined cyclic yield surface, i.e. Bauschinger reversed yield stress, was found to predict this first-cycle relaxation phenomenon with reasonable accuracy, and to yield residual stress values close to those measured using synchrotron X-ray diffraction. This lends credence to the notion that the mechanism for this relaxation is associated with localized yielding in the vicinity of the damage site, based on the monotonic or (where appropriate) reversed yield strength.
5) Spatial surface-normal strain maps, derived from in situ synchrotron X-ray diffraction measurements during loading, were consistent with a mechanism of first-cycle relaxation involving local plastic yielding caused by the superposition of the applied and residual stresses.
6) The relaxed residual stress state, combined with the product of the applied stress and appropriate stress-concentration factor at the damage site, provides a means to estimate the driving force for crack nucleation during subsequent HCF loading. This approach explains in large part the propensity for crack formation at the floor of the impact crater at high applied stresses ($\sigma_{max} \sim 0.5\sigma_y$) and at subsurface locations at lower applied stresses ($\sigma_{max} \sim 0.3\sigma_y$).

Acknowledgements

This work was supported by the US Air Force Office of Scientific Research under Grant No. F49620-96-1-0478 under the auspices of the Multidisciplinary University Research Initiative on High Cycle Fatigue to the University of California (for numerical modeling and fatigue analysis), the Office of Science, US Department of Energy under contract #DE-AC03-76SF00098 (for experimental diffraction results), and the Stanford Synchrotron Radiation Laboratory, operated by the Department of Energy, Office of Basic Energy Sciences (for X-ray beamtime). B.L. Boyce would like to thank the Hertz Foundation for their generous support in the form of a Hertz fellowship. Thanks are due to Dr J.M. McNaney for many helpful discussions.

References

[1] T. Nicholas, Int. J. Fatigue 21 (1999) S221.
[2] S.J. Hudak, Jr, K.S. Chan, R.C. McClung, G.G. Chell, Y.D. Lee, D.L. Davidson, High cycle fatigue of turbine engine materials, Final Technical Report, Southwest Research Institute, 31 August 1999.
[3] J.J. Ruschau, T. Nicholas, S.R. Thompson, Int. J. Impact Eng. 25 (2001) 233.
[4] J.O. Peters, B.L. Boyce, X. Chen, J.M. McNaney, J.W. Hutchinson, R.O. Ritchie, Eng. Fract. Mech. 69 (2002) 1425.
[5] B.L. Boyce, X. Chen, J.W. Hutchinson, R.O. Ritchie, Mech. Mater. 33 (2001) 441.
[6] J.O. Peters, R.O. Ritchie, Eng. Fract. Mech. 67 (2000) 193.
[7] J.O. Peters, R.O. Ritchie, Int. J. Fatigue 23 (2001) S413.
[8] H. Holzapfel, V. Schulze, O. Vöhringer, E. Macherauch, Mater. Sci. Eng. A248 (1998) 9.
[9] A. Wick, V. Schulze, O. Vöhringer, Mater. Sci. Eng. A293 (2000) 191.
[10] I. Altenberger, B. Scholtes, in: J. Kenny, A. Brebbia (Eds.), Surface Treatment IV, Southampton, UK, WIT Press, 1999.
[11] B.R. Sridhar, K. Ramachandra, K.A. Padmanabhan, J. Mater. Sci. 31 (1996) 4381.
[12] L. Wagner, G. Lütjering, in: H.O. Fuchs (Ed.), Proceedings of the Second International Conference on Shot Peening (ICSP-1), American Shot Peening Society, Paramus, NJ, 1984, p. 306.
[13] D. Eylon, Summary of the available information on the processing of the Ti–6Al–4V HCF/LCF program plates, University of Dayton Report, Dayton, OH, 1998.
[14] I.C. Noyan, J.B. Cohen, Residual Stress: Measurement by Diffraction and Interpretation, Springer, New York, 1987.
[15] P.S. Prevey, Advances in X-ray Analysis 20 (1977) 345.
[16] Hibbit, Karlsson and Sorensen Inc. ABAQUS version 5.7 User's Manual, Hibbit, Karlsson and Sorensen Inc., Pawtucket, RI, 1998.
[17] X. Chen, J.W. Hutchinson, Int. J. Fract. 107 (2001) 31.
[18] M.R. James, W.L. Morris, Scr. Metall. 17 (1983) 1101.
[19] W.L. Morris, R.V. Inman, M.R. James, J. Mater. Sci. 17 (1982) 1413.
[20] M. McClinton, J.B. Cohen, Mater. Sci. Eng. 56 (1982) 259.
[21] H. Kitagawa, S. Takahashi, Applicability of fracture mechanics to very small cracks or cracks in the early stage, in: Proceedings of the Second International Conference on Mechanical Behavior of Materials, ASM, Metals Park, OH, 1976, pp. 627–631.